Self-consistent determination of line-width and probe shape using atomic force microscopy

Eves, B. J.; Green, R. G.

Publisher's version / Version de l'éditeur:
https://doi.org/10.1088/0957-0233/24/8/085401
Measurement Science and Technology, 24, 8, pp. 1-10, 2013-07-02

Self-consistent determination of line-width and probe shape using atomic force microscopy

B J Eves and R G Green

National Research Council Canada, 1200 Montreal Road, Building M-36, Ottawa, Ontario, K1A 0R6, Canada

E-mail: Brian.Eves@nrc-cnrc.gc.ca

Abstract. A self-consistent method for determining line-width and probe shape using an atomic force microscope (AFM) has been developed. Through acquisition of three images in which one tip images the other, and each tip images the sample a least squares determination of the shapes of both tips, and the parameters that define the line-width standard can be determined. Application of the self-consistent method produces measurements that can be made traceable to the definition of the metre through appropriate calibration of the AFM. A comparison between the line-width determined by the method and a calibrated line-width standard shows good agreement. Sources of uncertainty specific to the self-consistent method are discussed.

Line-width, probe shape, atomic force microscopy, critical dimension

PACS numbers: 07.79.Lh, 06.20.Dk, 06.20.fb, 06.30.Bp

Submitted to: *Meas. Sci. Technol.*

1. Introduction

The measurement of line-width with an atomic force microscope (AFM) is complicated by the unknown shape and size of the probe. The available methods to characterize the probe either use artefacts of assumed size or shape [1–9], or use a technique called blind-tip estimation [10, 11]. The use of artefacts to determine probe shape requires an independent method of measurement to determine the artefact size/shape if traceability is to be established. Atomic resolution images from transmission electron microscopes (TEM) have been used to provide traceability of line-width artefacts to the definition of the metre based upon the silicon lattice constant [12, 13]. Unfortunately, the measured section of the artefact is rendered unuseable for subsequent AFM measurements during sample preparation for the TEM. Furthermore, the results of the TEM measurement are best compared to critical dimension AFM (CD-AFM) measurements that utilize special probes and scanning systems that result in the measured AFM line-width being a simple sum of the probe size and the artefact line-width. Few national metrology institutes have the resources to establish traceability in this manner. Other artefacts that have been used in the literature, such as spheres [1, 8], sharp protusions/tips [2, 4], and undercut plateaus [3, 5], rely upon assumptions on either their form or size that render the establishment of traceability difficult. An alternate traceability route independent of calibrated artifacts is a technique known as blind-tip estimation [10, 11]. It is a method to mathematically determine the largest possible probe that could have created an AFM image of an unknown surface. The determined probe shape can be used to generate a lower bound to the unknown surface while the AFM image represents an upper bound. The upper and lower boundaries can be used to provide an estimate of the measurement uncertainty for a particular measurand, *e.g.* line-width.

If AFM probes are perfectly spherical it is possible to self-consistently extract the probe radii for three different probes from the following series of measurements. Use three tips to generate three images of one tip imaging another such that all unique combinations are explored, *i.e.* tip A images tip B, tip B images tip C, and tip C images tip A. It is then trivial to extract the radii of the three spherical probes by solving the following system of three equations:

$$\begin{aligned} h_{\mathrm{AB}} &= r_{\mathrm{A}} + r_{\mathrm{B}} \\ h_{\mathrm{BC}} &= r_{\mathrm{B}} + r_{\mathrm{C}} \\ h_{\mathrm{CA}} &= r_{\mathrm{C}} + r_{\mathrm{A}} \end{aligned} \tag{1}$$

where h_{AB}, h_{BC}, and h_{CA} are the maximum heights measured from their respective images. If the probes are only close approximations to spheres then the location of the contact points between each non-ideal sphere must be properly accounted for. The physical rotation of the probes required to image one upon another complicates the task and the simplicity of equation 1 is lost [14]. A self-consistent technique has been successfully applied to non-ideal probes used with coordinate measurement machines [14], and has been used to determine the radius of curvature of AFM probes

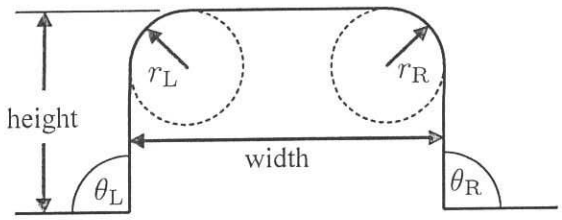

Figure 1. Line-width standard model indicating the fitting parameters.

by assuming perfect sphericity [3]. The probes used in AFMs are typically not spherical and it is an open question whether it is possible to extract from the three images the complete probe shapes necessary to accurately determine the width of an artifact.

To determine line-width and probe shape self-consistently a system comprising two AFM probes, tips A and B, and a line-width standard is studied. The line-width feature is treated like tip C in equation 1 so that the relevant set of measurements comprises tip A imaging tip B, and both tips A and B imaging the line-width feature. A mathematical model is developed to calculate a theoretical profile of tip A imaging tip B using the data of tip A and B imaging the line-width feature. This calculated profile is then fit to the experimental data of tip A imaging tip B by adjusting the line-width model parameters to yield the tip profiles and the line-width of the standard. The cross-section of the line-width standard is represented by a simple model and parameterized according to figure 1. The height of the line-width and the angle of the side-walls can be determined directly by measurement without influence from the probe shape. Therefore, the only parameters to be determined are the radius of curvature of the left and right corners and the line-width.

2. Theory

The process of image generation by an AFM can be described by the mathematical morphology operator of dilation [15, 16]

$$\begin{aligned} I(x,y) &= S(x,y) \oplus P(x,y) \\ &= \max_{x',y'}[S(x-x',y-y') + P(x',y')] \end{aligned} \tag{2}$$

where $I(x,y)$ is the generated image, $S(x,y)$ is the sample surface, and $P(x,y)$ is a transformation of the tip chosen to simplify notation and is related to the actual tip surface $T(x,y)$ by

$$P(x,y) = -T(-x,-y). \tag{3}$$

If the sample topography is known the probe shape can be extracted from the image by the erosion operator

$$\begin{aligned} P(x,y) &= I(x,y) \ominus S(x,y) \\ &= \min_{x',y'}[I(x+x',y+y') - S(x',y')]. \end{aligned} \tag{4}$$

The image formed of tip B when scanned by tip A is described by equation 2, or

$$I_{\mathrm{A,B}}(x,y) = S_{\mathrm{B}}(x,y) \oplus P_{\mathrm{A}}(x,y) \tag{5}$$

where $S_{\mathrm{B}}(x,y)$ is the surface of tip B after rotation by 180 degrees about the y-axis such that the tip is oriented correctly to be imaged by tip A (see figure 2). The relation between the rotated surface $S_{\mathrm{B}}(x,y)$ and the original tip surface $T_{\mathrm{B}}(x,y)$ is simply

$$S_{\mathrm{B}}(x,y) = -T_{\mathrm{B}}(-x,y), \tag{6}$$

where application of the variable transformation, equation 3, allows $S_{\mathrm{B}}(x,y)$ to be rewritten in terms of $P_{\mathrm{B}}(x,y)$, or

$$S_{\mathrm{B}}(x,y) = -T_{\mathrm{B}}(-x,y) = P_{\mathrm{B}}(x,-y). \tag{7}$$

The equation describing the image formed by tip B imaging tip A can now be written as

$$I_{\mathrm{A,B}}(x,y) = P_{\mathrm{B}}(x,-y) \ominus P_{\mathrm{A}}(x,y), \tag{8}$$

which can be further simplified by noting that tip profiles calculated via equation 4 are independent of the y-axis if the artifact being imaged is also independent of the y-axis. This is the case for an ideal line-width standard that only varies along the x-axis, and

$$I_{\mathrm{A,B}}(x) = P_{\mathrm{B}}(x) \oplus P_{\mathrm{A}}(x). \tag{9}$$

Approximations to the tip profiles $P_{\mathrm{A}}(x)$ and $P_{\mathrm{B}}(x)$ are generated via equation 4 given estimates to the line-width model parameters, or

$$P_{\mathrm{A}}(x) = I_{\mathrm{lp,A}}(x) \ominus S_{\mathrm{lp}}(x), \text{and} \tag{10}$$

$$P_{\mathrm{B}}(x) = I_{\mathrm{lp,B}}(x) \bigcirc S_{\mathrm{lp}}(x), \tag{11}$$

where the line profiles, $I_{\mathrm{lp}}(x)$, are extracted from images of the line-width feature taken with the AFM probes. Equations 9, 10, and 11 enable the calculation of the profile resulting from tip A imaging tip B. Comparison of the calculated profile with a measured surface profile of tip A imaging tip B enables the adjustment of the line-width parameters to minimize the error between the two curves, *i.e.* a least squares fitting process, and hence arrive at a self-consistent value for the line-width. It is important to understand that the erosion operators in equations 10 and 11 severely restrict the shape of the line-width structure. Its side-walls must be steeper than or equal to the side-walls of the tips such that the erosion operator can faithfully recreate the tip profiles.

Comparison of the calculated and measured surface profiles is complicated by the fact that the calculated result of equation 9 is inherently one dimensional, while the measurement result of tip A scanning tip B yields a two dimensional data set. It is therefore necessary to determine the subset of points from the measured image of tip B scanned by tip A that simultaneously match the contact points between each tip and the line-width feature. Specifically, the contact point on tip A that contributed to $I_{\mathrm{A,B}}(x_i, y_i)$ must be a contact point in image $I_{\mathrm{lp,A}}$. Furthermore, the contact point on tip B that contributed to $I_{\mathrm{A,B}}(x_i, y_i)$ must also be a contact point in image $I_{\mathrm{lp,B}}$. The

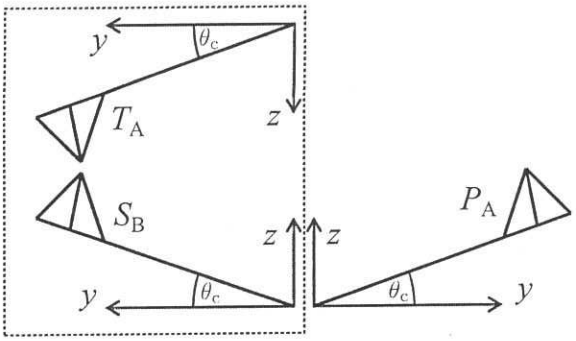

Figure 2. Relationship between the tip surfaces used to calculate the surface profile for tip A imaging tip B. The tip surfaces present within the physical experiment are enclosed by the dashed box.

line profile that satisfies these conditions is the maximum height along the y direction for every x point in the image and is given by

$$I^{\text{meas}}_{\text{A,B}}(x) = \max_y I^{\text{meas}}_{\text{A,B}}(x, y). \tag{12}$$

This assertion was tested and is shown to be accurate for specific tip geometries through computer simulations. The simulations use a simple algorithm to store the contact points on both the sample and the tip when calculating an image using the dilation operator. The model used to define the tips is based upon a rounded cone tilted at an angle (θ_c) to represent the mounting of the cantilever in the AFM as shown in figure 3. The tip apex is modeled by two halves of an ellipsoid (left side, and right side) such that an asymmetric tip is allowed. The cone angle can also vary from the left side to the right side. The line-width model previously presented in figure 1 again represents the sample. Calculated images of tip A (a), tip B (b), and their dilation with each other (c) are shown in figure 4. Table 1 lists the parameters used to generate figure 4. The location of the contact points calculated via equation 12 for the tip-on-tip image are marked by the red line in figure 4c. These contact points are mapped to both tip A and B via the modified dilation operator and are marked by a red line in figures 4a and 4b respectively. The dilation of tips A and B with the line-width feature are shown in figures 4d and 4e, while an image of the line-width model is shown in figure 4f. The blue dotted line in figures 4a and 4b are the contact points formed when tip A and B image the line-width standard (also calculated via the modified dilation operator). Clearly the contact points on the tips are the same when imaging either the line-width standard or another tip if equation 12 is used to generate the line-profile from the tip-on-tip image. Therefore, a comparison of the measured and calculated tip-on-tip surface profiles is valid for this particular case.

2.1. Implentation

To implement the self-consistent measurement scheme it is necessary to minimize alignment errors due to variation in the relative orientation of both tips and the line-

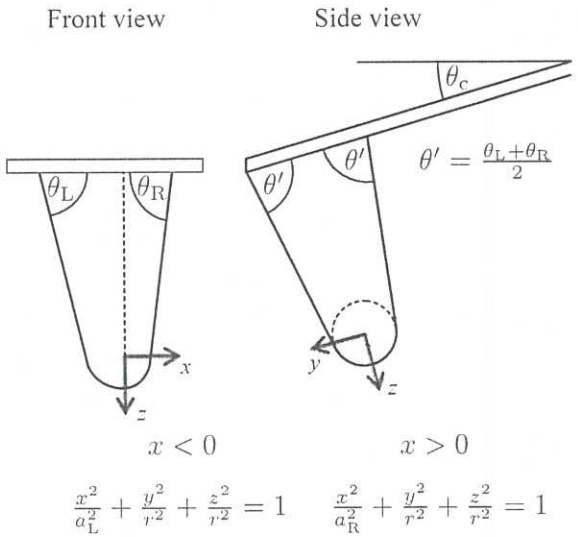

Figure 3. The model tip geometry used in the calculations.

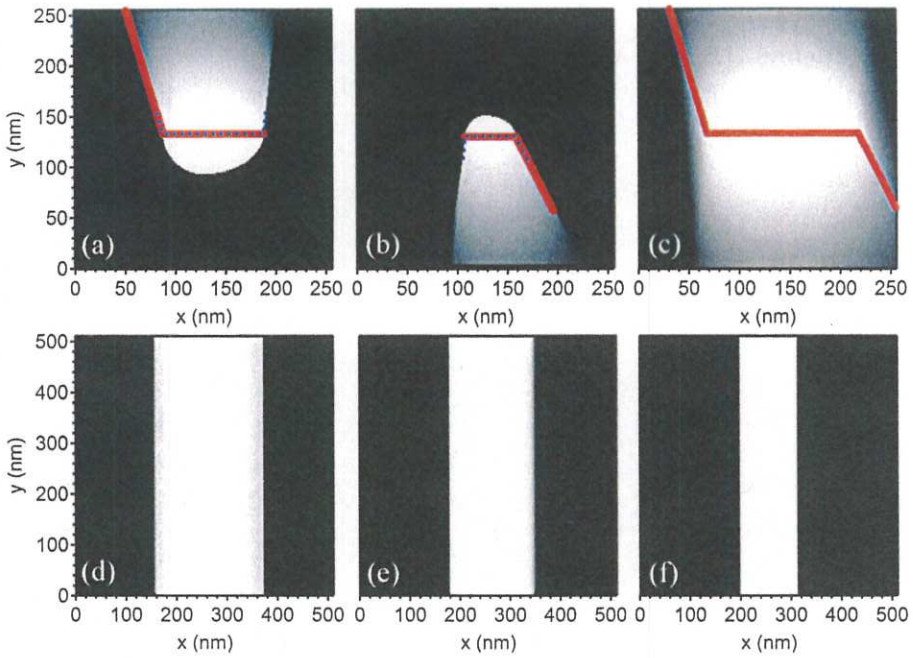

Figure 4. Calculated images of (a) tip A, (b) tip B, (c) dilation of tip A with tip B, (d) dilation of tip A with line profile, (e) dilation of tip B with line profile, and (f) the line profile. The red line in (c) are the locations of the maximum image height found for each x-value. The red line in (a) and (b) are the contact points calculated via a modified dilation operator for the maximum locations marked in (c). The blue dotted line in (a) and (b) are the contact points found for tips A and B imaging the line-width standard. The contact points on the tips are the same for imaging either the line-width standard or another tip.

Table 1. Parameters used to generate the line-width standard and the model tips.

	Line Profile
Height	160 nm
Left side-wall angle (θ_{L})	90 degrees
Left radius (r_{L})	3 nm
Width (w)	112 nm
Right radius (r_{R})	3 nm
Right side-wall angle (θ_{R})	90 degrees

	Tip A	Tip B
Cantilever angle (θ_{c})	10 degrees	10 degrees
Left cone angle (θ_{L})	89 degrees	85 degrees
Left major radius (a_{L})	60 nm	30 nm
Minor radius (r)	40 nm	20 nm
Right major radius (a_{R})	40 nm	20 nm
Right cone angle (θ_{R})	87 degrees	89 degrees

width standard. One method to reduce alignment errors is depicted in figure 5 and comprises three steps. First, image tip B using tip A as the probe (step 1). Leave tip A in position, replace tip B with the line-width standard, and capture the second image (step 2). Replace tip A with tip B while keeping the line-width standard in the same position (step 3), though it is likely that the standard will need to be moved a short distance to realign the tip above the line-width feature. Take final image. In the measurement scheme just described the orientation of tip B relative to tip A in step 1 and the placement of tip B into the AFM head in step 3 are the major source of alignment error. Imperfect 180 degree rotations of tip B that arise when changing the tip in step 3 are accounted for by an additional fitting parameter. The other alignment errors are minimized through experimental procedures as detailed in section 4.2.

Given the three images it is possible to extract a set of three line profiles (using equation 12 for the image of tip A on tip B) and use the algorithm in figure 6 to determine the line-width (w), the radius of curvature of the left (r_L) and right (r_R) sides of the line-width standard, and the rotation angle of tip B about the y-axis (α). The additional complexity of the algorithm, when compared to equations 9, 10, and 11, is a result of the book-keeping required to enable accurate calculation of the sum of the squares of the residuals between $I_{\mathrm{A,B}}^{\mathrm{meas}}$ and $I_{\mathrm{A,B}}^{\mathrm{calc}}$. Minimization of the least-squares error within the algorithm is accomplished via simulated annealing [17] as many local minima are present through out the searchable parameter space. Due to the random nature of the annealing process each parameter calculation is repeated ten times and obvious outliers are discarded. The average value and standard deviation of each parameter is reported.

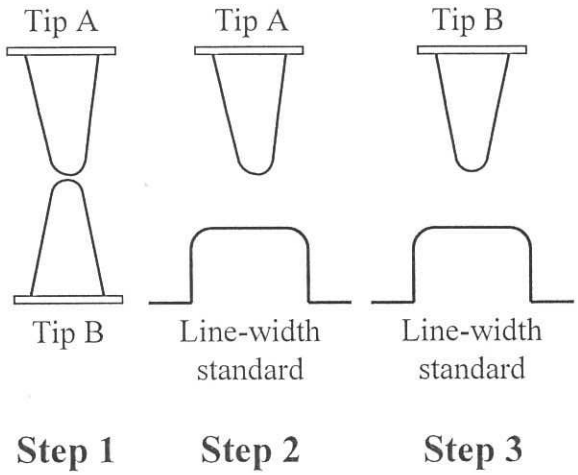

Figure 5. Measurement scheme to reduce alignment errors.

Input: $I_{\mathrm{lp,A}}(x)$, $I_{\mathrm{lp,B}}(x)$, $I^{\mathrm{meas}}_{\mathrm{A,B}}(x)$;
initialize r_L, w, r_R, and α;
$I^{\mathrm{meas}}_{\mathrm{A,B}}(x) = I^{\mathrm{meas}}_{\mathrm{A,B}}(x) - \max_x I^{\mathrm{meas}}_{\mathrm{A,B}}(x)$;
calculate 'centre of mass' $x_m = \sum_x x \cdot I^{\mathrm{meas}}_{\mathrm{A,B}}(x) / \sum_x I^{\mathrm{meas}}_{\mathrm{A,B}}(x)$;
while *error too big* **do**
    calculate line-width model $S_{lp}(x)$;
    calculate $P_A(x) = I_{\mathrm{lp,A}}(x) \ominus S_{\mathrm{lp}}(x)$;
    calculate $P_B(x) = I_{\mathrm{lp,B}}(x) \ominus S_{\mathrm{lp}}(x)$;
    rotate $P_B(x)$ about $x_r = \max_x P_B(x)$ by α;
    calculate $I^{\mathrm{calc}}_{\mathrm{A,B}}(x) = P_{\mathrm{A}}(x) \oplus P_{\mathrm{B}}(x)$;
    $I^{\mathrm{calc}}_{\mathrm{A,B}}(x) = I^{\mathrm{calc}}_{\mathrm{A,B}}(x) - \max_x I^{\mathrm{calc}}_{\mathrm{A,B}}(x)$;
    calculate 'centre of mass' $x_c = \sum_x x \cdot I^{\mathrm{calc}}_{\mathrm{A,B}}(x) / \sum_x I^{\mathrm{calc}}_{\mathrm{A,B}}(x)$;
    $error = (\sum_x (I^{\mathrm{meas}}_{\mathrm{A,B}}(x - x_m) - I^{\mathrm{calc}}_{\mathrm{A,B}}(x - x_c))^2)^{1/2}$;
    update parameters r_L, w, r_R, and α;
end

Figure 6. Algorithm used to calculate the unknown parameters of the model line-width standard.

3. Simulations

The line profiles associated with the simulated data displayed previously in figure 4 and the corresponding profiles after least squares fitting are shown in figure 7. The aggregate parameter results are published in table 2. The results agree excellently with the initial parameters and reproduce the tip profiles.

While it is clear the algorithm works well for certain realistic probe shapes its performance is not shape independent. Specifically probes that have a shallow side wall angle, such as pyramidal tips, result in sub-optimal fitting. Shown in table 3 are the

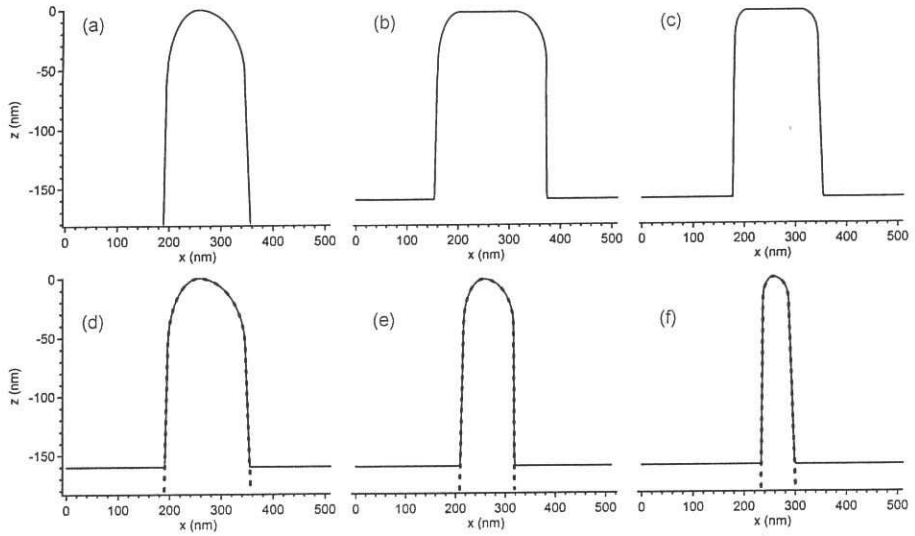

Figure 7. Line profiles detailing self-consistent determination of tip shape for model tips and line-width standard. Simulated line profiles of (a) tip A imaging tip B, and tips A and B imaging the line-width standard (b and c respectively). The results of the self-consistent calculation: (d) tip A imaging tip B (solid curve) and model data (dashed curve) for comparison, (e) tip A (solid curve) and model data (dashed curve) for comparison, and (f) tip B (solid curve) and model data (dashed curve) for comparison. The agreement between the self-consistent determination of the probe shapes and the model data validates the method.

Table 2. Line-width parameters as determined by the self-consistent method applied to simulated data. Parameters used to generate the simulated data can be found in table 1. Values are a result of 10 trial runs of which 2 where discarded as outliers.

	Actual	Calculated	Unit
Left radius (r_L)	3.00	3.02 ± 0.04	nm
Width (w)	112.00	112.01 ± 0.03	nm
Right radius (r_R)	3.00	3.02 ± 0.02	nm
Misalignment angle (α)	0.000	0.004 ± 0.005	degrees

results of applying the algorithm to a system that comprises a hemispherical tip and a line-width feature both with 90 degree sidewalls, and a pyramidal tip with 49 degree sidewalls. The shallow angles of the pyramidal tip do not constrain the solution as effectively.

4. Experiments

4.1. Apparatus

Atomic force microscopy measurements are performed using a modified Asylum MFP-3D‡ housed within an acoustic isolation enclosure. While the system operates in an

‡ NRC does not endorse or guarantee the performance of specific models of commercial equipment.

Table 3. Line-width parameters as determined by the self-consistent method applied to a system comprising a hemispherical tip and a line-width feature with 90 degree sidewalls, and a pyramidal tip with 49 degree sidewalls. Values are a result of 10 trial runs.

	Actual	Calculated	Unit
Left radius (r_L)	3.0	4.2 ± 1.1	nm
Width (w)	112.0	112.1 ± 0.8	nm
Right radius (r_R)	3.0	4.4 ± 1.0	nm
Misalignment angle (α)	0.00	-0.4 ± 1.0	degrees

environmentally controlled laboratory (20 °C±0.05 °C, RH 30%±2%), normal operating conditions within the enclosure typically stabilize to 23 °C at 28% RH as a result of instrument self-heating. Modifications to the AFM integrate a stack of four nano-positioning stages (Attocube Systems AG) to provide sample positioning within a 5 x 5 x 5 mm^3 volume and 360 degrees of rotation about the instrument z-axis. The stages mount on the AFM x/y flexure stage and move with the sample during imaging. They are used for precise sample and tip alignment without the need for manual manipulation which disturbs the thermal stability of the system. The x and y scanning motion of the AFM is decoupled from the z-scanner which is integrated onto a removable head. The head kinematically mounts above the x/y scanner during imaging. Cantilevers clamp onto holders, which also kinematically mount to the z-scanner thus providing reproducible positioning. For tip-on-tip measurements a second cantilever holder is mounted to the top of the nano-positioning stack. The scales of the AFMs integrated x/y position sensors (linear variable differential transducers or LVDTs) are calibrated using NRC fabricated grating pitch standards that are traceable via diffractometer measurements [18] to the definition of the meter. The integrated LVDT on the z-scanner is calibrated directly via interferometry.

The cantilevers utilized in the experiments are listed in table 4. Wear resistant tungsten carbide coated tips are used to minimize changes in the probe morphology, and the AFM scan parameters are chosen to reduce the magnitude of the tip-sample forces. In most cases this is sufficient to prevent significant wear over the course of one or several measurement cycles. The static deflection of the AFM cantilever during a tip-on-tip measurement is found to vary significantly. The deflection change occurs when moving from the flat portion of the cantilever to the tip apex and is not simply due to imaging on a compliant surface but is correlated to surface geometry. The cantilever of tip A is chosen to have a small spring constant relative to the spring constant of tip B so as to minimize possible static deflection due to surface compliance. The cantilevers also have different resonant frequencies to reduce the transfer of energy between the two oscillators. The line-width structure is orientated perpendicular to the cantilever long-axis in order to minimize oscillations attributed to friction [19].

Table 4. Nominal characteristics of the cantilevers used in the self-consistent measurement of line-width.

	Tip A	Tip B
Manufacturer	Team Nanotec GmbH	Team Nanotec GmbH
Model	HSC-20-225C3.0-MC	HSC-4-125C40-MC
Resonant Frequency	70 kHz	300 kHz
Spring Constant	4 N/m	30 N/m
Tip Radius	20 nm	40 nm
Shape	hemispherical conical	hemispherical conical
Coating	tungsten carbide	tungsten carbide

4.2. Methodology

The self-consistent measurement of line-width requires three separate measurement steps as previously shown in figure 5. For consistent results it is important that the contact points between the AFM tips in step 1 are the same as those used to image the line-width standard in the subsequent steps. Cantilever misalignment, and thermal drift can each cause deviations in the contact points, therefore procedures were developed to minimize these contributions and represent current best practice.

Initially both cantilevers are mounted on kinematic holders and aligned by eye or under a 10X eye piece. Subsequently, each holder is mounted on the AFM z-scan head and viewed for alignment in the integrated microscope; any adjustments required are performed by removing the holder and readjusting. The microscope axes are known to be well aligned with the x/y-scan axes from previous experiments. After each cantilever is verified to be aligned in its holder, tip A is mounted on the z-scan head and tip B on the sample stage (see figure 8). The alignment of tip B to the AFM x-axis for step 1 is more difficult due to reduced visibility in the microscope, however its orientation can be verified by acquiring an AFM image at the edge of the cantilever and adjusting if necessary via the sample rotary stage. Cantilever alignment to the scanner x-axis is typically better than $\pm 2^\circ$.

Thermal drift of the cantilever relative to the sample is an important source of error in the measurements. It is minimized by allowing extended periods of stabilization after turning on the system, or changing the tips or sample. Typical stabilization times are about 12-18 hours when turning on the system for the first time, and 3 to 6 hours when changing the sample or tip. The temperature stability is monitored through thermistors mounted in the enclosure and at various locations around the AFM, including by the sample holder. Software continuously monitors the temperature, cantilever oscillation amplitude, and cantilever deflection signals. Imaging commences when all signals plateau, however, once scanning is initiated the AFM warms slightly and an increase in thermal drift occurs. This is especially important for tip-on-tip imaging, and to mitigate this while avoiding excessive tip wear, the AFM is scanned without the tip in contact with the sample while still following an approximation of the sample topography. The

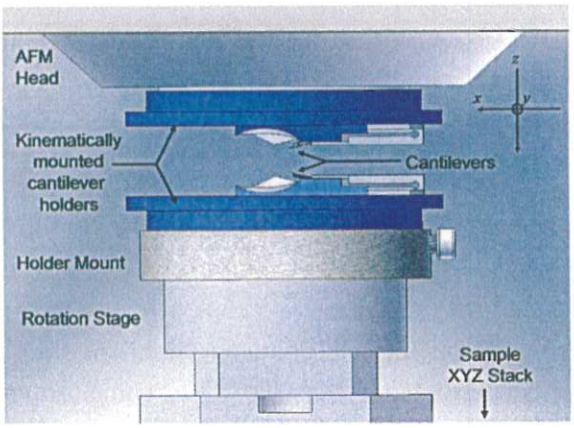

Figure 8. Schematic representation of the experimental setup for step 1. Tip A is shown mounted to the AFM z-scanner while tip B is coupled to the stack of nano-motion stages used for positioning.

apex of the tip is first imaged at low resolution in the slow scan direction (4096 x 16), the data from the scan line covering the image maximum is then used to build an artificial image of higher resolution (typically 4096 x 256). The data from this artificial image is then fed into the AFM scan engine, to simulate a true scan. The tip is kept away from the surface by offsetting each z coordinate in the simulated scan by about 5 μm from the maximum of the true sample position. The scanner is exercised for a minimum of four hours before the final set of images are acquired for step 1. Consecutive images are acquired and used to calculate the drift speed of the maximum point. Only when this speed is below approximately 2 nm/min is the drift considered to be sufficiently low to proceed to steps 2 and 3. The overall measurement procedure is summarized in the flow chart in figure 9.

4.3. Results

The images, associated line profiles, and results after application of the self-consistent line-width algorithm are shown in figure 10 for data acquired using the probes listed in table 4, and a 112 nm wide line-width standard (VLSI Standards Inc. Model NCDMO-110). No smoothing was applied to the data. The number of data points in the line profiles was reduced from 4096 points to 400 points via interpolation and decimation in order to reduce computation time. Figure 10g shows excellent agreement between the calculated (via the algorithm listed in figure 6) and measured tip-on-tip line profiles with only the apex of the profiles showing any obvious disagreement. Simulations verify that the flattening at the apex of a calculated tip-on-tip line profile occurs when the input height of the line-width standard used in the least-squares fitting process is smaller than the actual height of the standard. The profiles of the standard (figures 10c and 10f) reveal that the top is not flat but concave. The difference observed in figure 10g is therefore attributed to the underestimation of the line-width height due to deviations

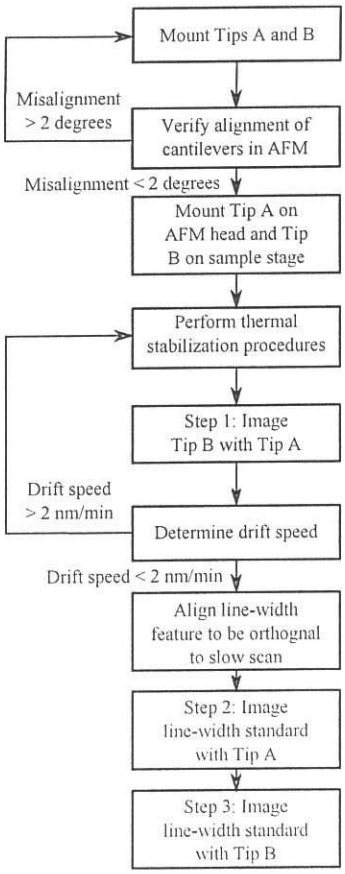

Figure 9. Flow chart describing the measurement scheme including drift minimization procedures.

from the assumed model. The calculated profiles of both tip A and B are shown in figures 10h and 10i.

The calculated line-width for five independent self-consistent measurements is shown in figure 11. The measurements, acquired over several months, used the same line-width standard but each used a different combination of tips. Multiple tip-on-tip images and five line-profiles from each line-width measurement are used to calculate a single line-width value. Each image also included trace and retrace data which were analysed separately but averaged to yield a single line-width value. The mean and standard deviation of the five measurements is 111.8 ± 2.0 nm which agrees with the calibrated value (95% confidence level) of 112.4 ± 0.8 nm. Note that the definition of the two measurands are different as the calibrated value is based upon a set of distributed measurements while the presented measurements are roughly localised to one section of the standard. However, this is not thought to be significant as the reported spatial variation of the calibrated line-width has a combined standard deviation of 0.5 nm. A consistent difference of ~ 1 nm exists between the line-width results for trace and retrace line profiles. The difference is likely due to the asymmetry in the response of the AFM to rising and falling edges.

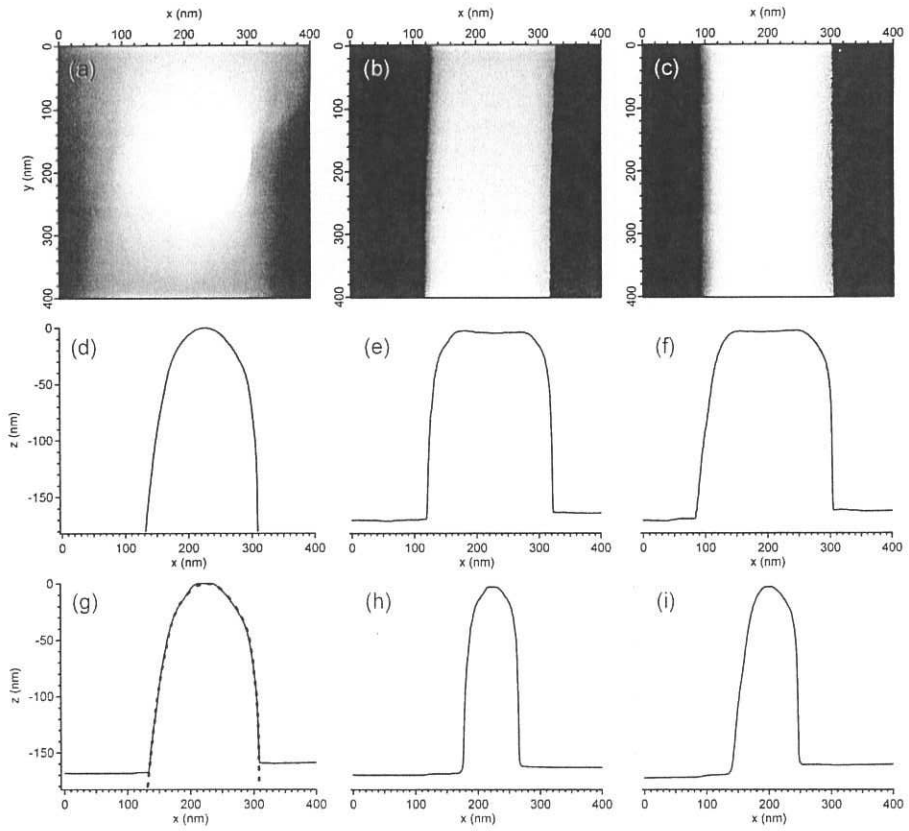

Figure 10. Experimental images, and associated line profiles and results after application of the self-consistent line-width algorithm: (a) tip A imaging tip B, (b) tip A imaging line-width standard, (c) tip B imaging line-width standard, (d) line profile extracted from image of tip A upon tip B, (e) line profile of tip A imaging line-width standard (f) line profile of tip B imaging line-width standard, (g) calculated profile of tip A imaging tip B (solid) compared with experimental data (dashed), (h) calculated profile of tip A, and (i) calculated profile of tip B. Grayscale in (a) extends over 1593 nm. Grayscale in (b) extends over 227 nm. Grayscale in (c) extends over 178 nm. Good agreement exists between the self-consistent method and the measured tip-on-tip profile.

The calculated values for the left and right radii of the line-width standard and the misalignment angle α can vary greatly within the calculated solutions for a set of images. For example, the line-profile radii (see figure 1) can have a spread of values greater than 10 nm even though the calculated line-width has a spread of values less than a nanometre. The constraints imposed by the least-squares fitting process does not seem to sufficiently restrict the values for the radii or the misalignment angle and care should be taken in their interpretation.

4.4. Sources of uncertainty

There are many sources of uncertainty that affect the measurement capabilities of an AFM [20] and hence the determination of line-width and probe shape. Only those

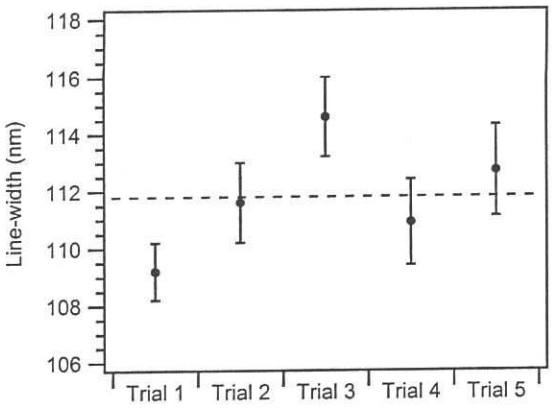

Figure 11. Line-width measurement results using the self-consistent method for five independent trials of a critical dimension standard. The average value is shown (dashed curve) and agrees with the calibrated line-width value.

sources that are significant and of particular interest in the application of the self-consistent method are considered.

The orientation of the probe before and after rotation (see figure 5) is an obvious source of uncertainty and simulations have been performed to study the contribution. The tips and line-width described in table 1 were used to simulate tip-on-tip images that had been perturbed via rotations of one of the tips. Rotations of tip B about the x-axis (see figure 2) do not result in any changes in the tip-on-tip line profiles and is expected given the spherical nature of the end of the simulated tips. However, this is not likely to remain true for actual probes which have deviations from spherecity at the tip apex. Misalignment of the cantilever about the y-axis is compensated for by the fitting parameter α as discussed previously in section 2.1. Rotations up to $\pm 8^\circ$ of tip B about the z-axis induce changes of less than 0.2 nm in the measured line-width. The increase in rotation about the z-axis directly correlates to an increase in the fitting parameter α, but is not correlated to line-width. The misalignment of one of the probes does not appear to significantly affect the line-width measurement if probes with hemispherical apexes are used. Experimental determination of the alignment sensitivity is required due to non-ideal tip geometries.

Thermal drift is a potential source of uncertainty that is of particular interest when performing tip-on-tip measurements. To reduce following error while measuring the steeply angled sidewalls present in the tip-on-tip images the scan speed is limited to speeds around 100 nm/s, and the acquisition time for a single image is approximately 35 minutes. To study the effects of drift a series of 26 tip-on-tip images covering a span of 14 hours are analysed. The coordinates of the maxima of the tip-on-tip images are used as a reference point in each image and used to measure the drift. The coordinate data for the maxima are shown in figure 12. Over the 14 hour period substantial drift is observed in all three axes, with the greatest component along the z-axis. Furthermore

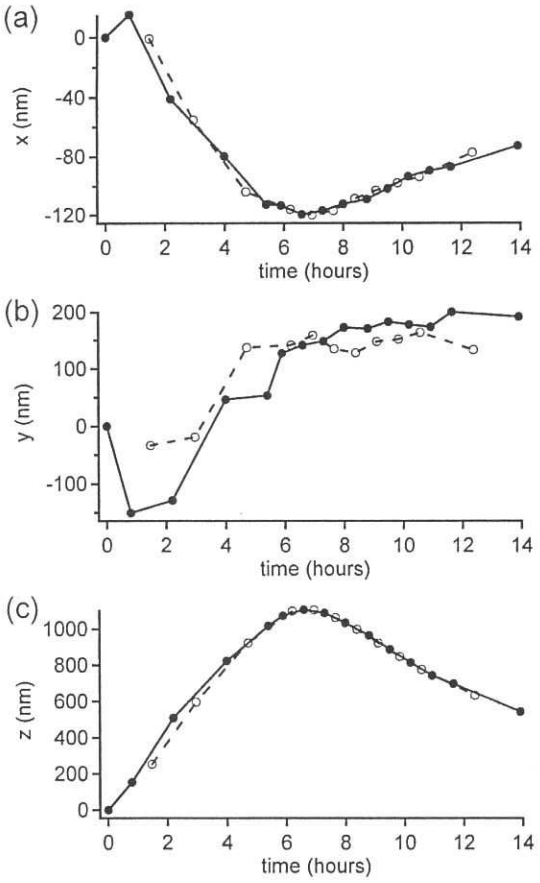

Figure 12. Coordinates of the maxima from consecutive tip-on-tip images reveal the magnitude of drift experienced by the AFM: (a) x, (b) y, (c) z. Maxima from scan down images are connected via a solid line, while maxima from scan up images are connected via a dashed line.

the drift velocity is not constant and even changes sign halfway through for two of the three axes. The same tip-on-tip images used to track drift are also used to generate self-consistent line-width values and these are plotted in figure 13a. The error in the fitting results (figure 13b) over the first six hours are correlated to instability in the measured line-width value. The rate of drift is greatest during this period. The instability that occurs for times greater than or equal to 12 hours does not correlate with either the error or the rate of drift along any axis. Shown in figure 13c is the distance measured between consecutive image maxima if and only if a change in slow scan direction occured. The distance between consecutive image maxima appears to be a good predictor of stable self-consistent line-width results. For distances less than 60 nm the self-consistent line-width values have a standard deviation of 0.2 nm. Further study is required to determine whether this correlation holds for other data sets and to ascertain a suitable threshold value. The distance between consecutive image maxima is obviously related to the magnitude of the AFM drift, but it is unclear whether other processes influence the measured distance values.

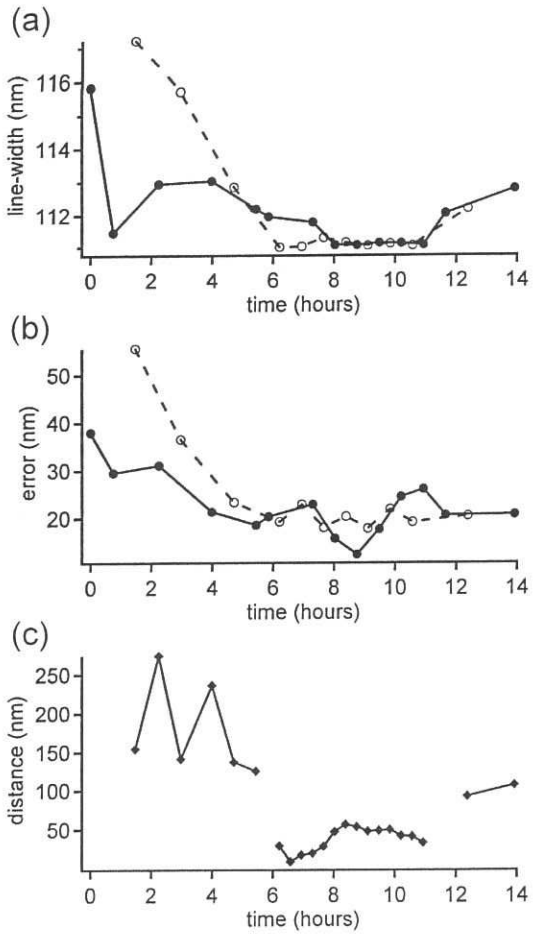

Figure 13. Self-consistent line-width results using consecutive tip-on-tip images. The calculated line-width (a), and the least-squares fitting error (b) are compared to the distance between consecutive image maxima (c). Scan down images in (a) and (b) are connected via a solid line, while the dashed line connects scan up images. Short distance between consecutive image maxima correlates to consistent line-width values.

An assumption made during development of the self-consistent theory is that the line-width sample is uniform along its entire length. For real samples this is not true and variations in line-width should be accounted for. The non-uniformity enters into the calculation via the two line profiles extracted from tips A and B imaging the line-width standard. If the two line profiles do not sample exactly the same section of the line-width standard then an error in the calculated line-width occurs. To evaluate this error the line-width calculation was performed for every scan line comprising an image of tip A scanning the line-width standard (figure 10b) and a single scan line for tip B imaging the line-width standard (figure 10f). The results are plotted in figure 14. Note that the average value of 110.4 nm has been subtracted and the residuals are plotted. Also plotted are the residuals for line-width values calculated by measuring the distance between the points of the profile 50% below the top of the line-width structure. The average value between points is 194.7 nm. There is good agreement between the two

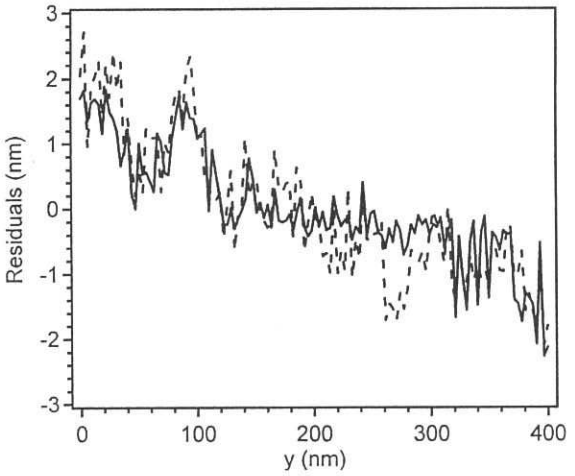

Figure 14. Variation of line-width measured by self-consistent algorithm (solid curve) and line-width calculated via distance between level-crossings at 50% below top of line-width structure (dashed curve). Residuals, *i.e.* deviation from average, are plotted.

data sets of residuals which implies that a 1 nm change in line-width in one image will result in a 1 nm change in the calculated line-width. This is unexpected since calculations using simulated data predict that a 1 nm change in line-width in one image induces a 0.5 nm change in the calculated line-width. The difference is likely a result of limitations in the least-squares fitting process when applied to experimental data that approximately conforms to the model.

5. Conclusion

A new method for the determination of line-width and probe shape has been developed. It is self-consistent and only requires that the line-width feature be well represented by a simple model equation. The traceability for the measurement is through the calibrated instrument scales of the AFM rather than through a secondary standard. While further work is required to understand and reduce the dominant sources of uncertainty, drift has been shown to be a major contributor. Techniques have been developed to minimize drift in a commercial instrument, but the thermal stability offered by metrological AFMs could reduce this further and greatly simplify the measurement process. The self-consistent line-width method generates tip profiles of one dimension. This is a limitation when determining the full probe shape and has been imposed by the choice of a one-dimensional artefact, *i.e.* the line-width standard. It can be removed by a suitable choice of two dimensional standard. The self-consistent determination of the complete AFM probe shape is therefore possible and will be pursued in future work.

References

[1] V.J. Garcia, L. Martinez, J.M. Briceno-Valero, and C.H. Schilling. Dimensional metrology of

nanometric spherical particles using AFM: I, model development. *Probe Microscopy*, 1(1):107–116, 1997.

[2] G.W. Bao and S.F.Y. Li. Characterization of atomic force microscopy (AFM) tip shapes by scanning hydrothermally deposited ZnO thin films. *Talanta*, 45(4):751–757, 1998.

[3] F. Meli. Critical dimension (CD) measurements using a metrology AFM profiler. In K. Hasche, W. Mirandé, and G. Wilkening, editors, *Quantitative Microscopy, Proceedings of the 4th Seminaor on*, pages 58–65. PTB-Bericht PTB-F-39, 2000.

[4] B. Skårman, L.R. Wallenberg, S.N. Jacobsen, U. Helmersson, and C. Thelander. Evaluation of intermittent contact mode AFM probes by HREM and using atomically sharp CeO2 ridges as tip characterizer. *Langmuir*, 16(15):6267–6277, 2000.

[5] U. Hübner, W. Morgenroth, H.G. Meyer, T. Sulzbach, B. Brendel, and W. Mirandé. Downwards to metrology in nanoscale: Determination of the AFM tip shape with well-known sharp-edged calibration structures. *Applied Physics A: Materials Science and Processing*, 76(6):913–917, 2003.

[6] H. Itoh, T. Fujimoto, and S. Ichimura. Tip characterizer for atomic force microscopy. *Review of Scientific Instruments*, 77(10), 2006.

[7] T. Machleidt, K.-H. Franke, H. Romanus, V. Cimalla, M. Niebelschtz, L. Spieß, and O. Ambacher. Using defined structures on very thin foils for characterizing AFM tips. *Ultramicroscopy*, 107(10-11):1086–1090, 2007.

[8] Z.-g.Zeng, G.-d. Zhu, Z. Guo, L. Zhang, X.-j. Yan, Q.-g. Du, and R. Liu. A simple method for AFM tip characterization by polystyrene spheres. *Ultramicroscopy*, 108(9):975–980, 2008.

[9] T. Inaba, J. Xie, R. Sugiyama, and Y. Homma. Tip characterizer for atomic force microscopy using singly suspended carbon nanotube. *Surface and Interface Analysis*, 44(6), 2012.

[10] J.S. Villarrubia. Morphological estimation of tip geometry for scanned probe microscopy. *Surface Science*, 321(3):287–300, 1994.

[11] J.S. Villarrubia. Algorithms for scanned probe microscope image simulation, surface reconstruction, and tip estimation. *Journal of Research of the National Institute of Standards and Technology*, 102(4):425–454, 1997.

[12] R. Dixson and N.G. Orji. Comparison and uncertainties of standards for critical dimension atomic force microscope tip width calibration. In *Proceedings of SPIE - The International Society for Optical Engineering*, volume 6518, 2007.

[13] N.G. Orji, R.G. Dixson, D.I. Garcia-Gutierrez, B.D. Bunday, M. Bishop, M.W. Cresswella, R.A. Allen, and J.A. Allgair. Tem calibration methods for critical dimension standards. In *Proceedings of SPIE - The International Society for Optical Engineering*, volume 6518, 2007.

[14] A Küng, F Meli, and R Thalmann. Ultraprecision micro-CMM using a low force 3D touch probe. *Measurement Science and Technology*, 18(2):319–327, 2007.

[15] G.S. Pingali and R. Jain. Restoration of scanning probe microscope images. In *Applications of Computer Vision, Proceedings, 1992., IEEE Workshop on*, pages 282–289, 1992.

[16] D.J. Keller and F.S. Franke. Envelope reconstruction of probe microscope images. *Surface Science*, 294(3):409–419, 1993.

[17] A. Corana, M. Marchesi, C. Martini, and S. Ridella. Minimizing multimodal functions of continuous variables with the "simulated annealing" algorithm. *ACM Transactions on Mathematical Software*, 13(3):262–280, 1987.

[18] B.J. Eves, J.R. Pekelsky, and J.E. Decker. Uncertainty evaluation of the nrc imaging diffractometer. *Measurement Science and Technology*, 19(7), 2008.

[19] B.J. Eves and R.G. Green. Limitations on accurate shape determination using amplitude modulation atomic force microscopy. *Ultramicroscopy*, 115:14–20, 2012.

[20] V. Korpelainen and A. Lassila. Calibration of a commercial afm: Traceability for a coordinate system. *Measurement Science and Technology*, 18(2):395–403, 2007.